RSC Advances

PAPER

View Article Online
View Journal | View Issue

Cite this: *RSC Adv.*, 2026, **16**, 15361

Engineered $SrSnFe_2O_4$@δ-MnO_2/activated biochar heterocomposite with a porous surface for efficient *o*-nitrophenol removal

Ahmed M. Abdelfatah, *[a] Mohamed E. El-Khouly,[b] Abdelazeem S. Eltaweil [cd] and Manal Fawzy[a]

Water contamination by phenolic compounds remains a critical environmental challenge, requiring adsorbents that combine high efficiency, structural stability, and facile recovery. In this study, we report a novel heterostructured composite, $SrSnFe_2O_4$@δ-MnO_2/BC_{KOH}, synthesized from cotton-branch-derived biochar through sequential KOH activation, MnO_2 growth, and magnetic ferrite incorporation. Unlike conventional MnO_2/biochar systems, the incorporation of $SrSnFe_2O_4$ induced α-to-δ MnO_2 phase transformation, heterointerface strain, and defect formation, enhancing surface functionality and adsorption reactivity. Comprehensive characterization (SEM, XRD, BET, XPS, VSM) confirmed a highly porous carbon framework, abundant oxygen-containing groups, and strong magnetic properties (M_s = 54.87 emu g^{-1}), enabling efficient pollutant capture and rapid magnetic separation. The composite exhibited excellent adsorption of *o*-nitrophenol (*o*-NP), achieving 99.04% removal within 60 min and a maximum adsorption capacity of 525.51 mg g^{-1}. Adsorption followed the Freundlich isotherm and pseudo-second-order kinetics, and XPS analysis revealed synergistic interactions between surface functionalities and *o*-NP molecules. The material maintained good reusability (50.29% after five cycles) and demonstrated effective removal in real wastewater samples. This work presents a scalable strategy for constructing magnetically retrievable δ-MnO_2/biochar heterostructures with superior adsorption performance, highlighting their potential for practical wastewater remediation.

Received 12th January 2026
Accepted 8th March 2026

DOI: 10.1039/d6ra00303f

rsc.li/rsc-advances

1. Introduction

Environmental pollution has become a serious issue over the last few decades. One primary reason is rapid industrial growth and the continuous release of wastewater.[1] These effluents often contain toxic organic compounds that can harm aquatic life and pose risks to human health.[2,3] One of the most hazardous pollutant categories is nitrophenols due to their toxicity and stability. They are commonly present in wastewater from petrochemical and oil-refining operations, plastics and paint industries, leather processing, pharmaceutical production, photographic activities, steel manufacturing, and olive oil processing.[4] Because of their stable aromatic structure and the presence of nitro groups, nitrophenols are difficult to biodegrade and can persist in water for long periods.[4] As a result, strict limits have been proposed or applied for phenolic contaminants in industrial discharges and drinking water.[4] Regulatory agencies have imposed strict discharge limits; for example, the U.S. EPA sets a maximum allowable concentration of 0.5 mg L^{-1} of phenol in industrial effluents,[5] while the World Health Organization (WHO) recommends a much lower threshold of 0.001 mg L^{-1} in drinking water.[6] Various methods have been reported for the removal of phenolic compounds from industrial effluents, including photocatalytic oxidation, electrochemical oxidation, chemical oxidation, adsorption, and microbiological processes.[5–7] Among treatment techniques, adsorption is notable for its simplicity, high efficiency, low risk of secondary pollution, and potential for adsorbent regeneration.[8]

Biochar (BC) is an effective carbon material widely used for adsorption because it is low-cost, sustainable, and structurally versatile. Activating BC (especially with KOH) develops a more open, hierarchical pore network that allows pollutants to enter quickly and be retained through pore filling and various physical interactions.[9,10] Moreover, the aromatic domains of BC provide favourable sites for π–π stacking with phenolic rings, while oxygen-containing groups can provide additional stabilization through hydrogen bonding.[10] These merits enable BC to provide rapid, early-stage uptake, transferring *o*-NP from solution to the solid interface. Although BC provides rapid physical

[a]*Green Technology Group, Environmental Sciences Department, Faculty of Science, Alexandria University, Alexandria 21511, Egypt. E-mail: AhmedMohamedFatah@alexu.edu.eg*

[b]*Nanoscience Program, Faculty of Basic and Applied Sciences, Egypt-Japan University of Science and Technology, New Borg El-Arab City, Alexandria, Egypt*

[c]*Department of Engineering, College of Engineering and Technology, University of Technology and Applied Sciences, Ibra, Sultanate of Oman*

[d]*Department of Chemistry, Faculty of Science, Alexandria University, Alexandria, Egypt*

capture, this interaction alone may be insufficient to ensure strong and stable adsorption as equilibrium is approached.[11] Therefore, metal oxides such as MnO_2 can be introduced to provide a high density of reactive surface sites, and their variable manganese oxidation states enhance interfacial activity.[12] One of the more attractive forms of MnO_2 is δ-MnO_2 because its layered structure and oxygen-rich surface provide strong interfacial interactions and facilitate charge redistribution. Beyond conventional MnO_2 forms, δ-MnO_2 offers additional advantages due to its high density of oxygen vacancies and rapid surface redox activity, which enhance ion exchange, surface complexation, and interfacial electron transfer.[13]

Recent studies have explored the incorporation of MnO_2 onto biochar to enhance adsorption and catalytic performance; however, most reported MnO_2/biochar composites rely on simple physical mixing or surface deposition, which often results in weak interfacial contact and limited electron-transfer efficiency.[14] In contrast, the heterostructure developed in this work introduces a unique interfacial coupling between MnO_2 and the carbon matrix through an *in situ* growth mechanism, producing a highly integrated MnO_2-carbon interface. This architecture provides hierarchical porosity, stabilized manganese oxidation states, and improved redox cycling, collectively enhancing the material's catalytic and adsorption behaviour. Moreover, using agricultural-waste-derived biochar and a green, low-temperature synthesis route distinguishes this system from conventional composites and contributes to its sustainability. These features highlight the novelty of the proposed heterostructure and its advantages over existing MnO_2/biochar materials.[15]

Despite extensive studies of carbon–metal oxide hybrid adsorbents, significant limitations remain. Many reported systems suffer from limited regeneration, insufficient active sites, and weak or unstable magnetism, which hinder their practical applicability. In particular, most ferrite-biochar composites exhibit suboptimal affinity for phenolic pollutants due to low redox activity, inadequate surface functionality, or poor pore accessibility, while their structural robustness under repeated cycles is often insufficient. These gaps highlight the need for multi-functional, magnetically recoverable hybrid adsorbents that combine strong interactions with phenolic molecules, structural stability, and efficient reusability.[16] To address these challenges, magnetic properties can be enhanced by incorporating metals or multi-cationic ferrites into carbon matrices. $SrSnFe_2O_4$ offers distinct advantages over conventional ferrites: as a multi-cationic M-type ferrite, it contains Sr^{2+} and Sn^{4+} ions, which introduce lattice distortion, increase the density of Lewis-acidic sites, and enhance electron-acceptor properties. These features strengthen interactions with phenolic –OH and $-NO_2$ groups compared with simpler ferrites such as Fe_3O_4. Additionally, the Fe^{3+}/Fe^{2+} redox pair can facilitate electron exchange and surface complexation. When combined with δ-MnO_2 and activated biochar, $SrSnFe_2O_4$ forms a complementary heterostructure with abundant active sites, enhanced interfacial electron transfer, strong π–π interactions, and hierarchical pore filling, resulting in a high-performance hybrid adsorbent for *o*-nitrophenol and other phenolic pollutants.[17–19]

This study demonstrates the successful development of a novel, sustainable $SrSnFe_2O_4$@δ-MnO_2/BC_{KOH} heterostructure derived from cotton branch biomass (*Gossypium barbadense*). The composite effectively integrates the magnetic and Lewis-acidic properties of $SrSnFe_2O_4$, the high surface reactivity and layered structure of δ-MnO_2, and the mesoporous, high-surface-area architecture of activated biochar. The work shows that this heterostructure achieves rapid and efficient *o*-nitrophenol adsorption, with enhanced interfacial interactions and synergistic effects between components. Additionally, the material exhibits excellent structural stability and reusability, facilitated by its strong magnetic properties, making it a promising candidate for practical wastewater remediation applications. These findings provide new insights into the design of multi-functional, magnetically recoverable biochar-based composites with superior adsorption performance.

2. Materials and methods

2.1. Chemicals

All chemicals and reagents used in this study were of analytical grade, as detailed in SI Text S1.

2.2. Plant extract preparation

Cotton branches (*Gossypium barbadense*) were collected from the El-Mamoura agricultural area near Alexandria, Egypt, with fresh biomass obtained from the Agriculture Research Centre (ARC) experimental farm. The branches were thoroughly washed with tap and distilled water, dried at 60 °C, and ground into a fine powder using a stainless–steel mill. For extract preparation, the powder was suspended in distilled water at a 10% (w/v) solid-to-liquid ratio, heated at 70 °C with gentle stirring for 20 min, and then filtered through Whatman No. 1 paper. The resulting filtrate was stored in sterilized Falcon tubes at 4 °C for subsequent use.

The selection of cotton branches as the botanical source was based on their well-documented richness in bioactive phytochemicals that serve as natural reducing and stabilizing agents in green nanoparticle synthesis. Literature on *Gossypium species* reports the presence of monoterpenes, sesquiterpenes, triterpenes, phenolic acids and their analogues, flavonoids, tannins, coumarins, as well as fatty acids, carbohydrates, and proteins.[20–22] These biomolecules are known to participate in electron donation, metal chelation, and nanoparticle capping, thereby facilitating controlled nucleation and preventing agglomeration during the formation of metal oxide and ferrite nanoparticles. The extraction conditions used in this study (70 °C, 20 min, and 10% w/v) were selected based on established green-synthesis methodologies, which demonstrate that such parameters effectively release active phytochemicals while preventing their thermal degradation.

2.3. Two-step cotton branches biochar activation *via* KOH

Biochar was prepared following a modified version of a previously reported procedure.[23] Dried cotton branch powder (50 g) was pyrolyzed in a horizontal tubular furnace at 450 °C for 1 h

under N_2 flow (100 mL min^{-1}), using a heating rate of 10 °C min^{-1}. After cooling under nitrogen, the biochar was washed with ethanol, acid-treated with 0.1 M HCl (1 : 10, v/v) for 24 h and rinsed with distilled water to neutral pH. The product was dried at 60 °C overnight, yielding ~50% biochar, consistent with reported values for lignocellulosic biomass at similar temperatures. For chemical activation, 10 g of cotton branch biochar was soaked in 100 mL of 3 M KOH (KOH : biochar = 3 : 1, w/w) for 24 h. The impregnated biochar was washed, filtered, and dried at 60 °C for 6 h, then pyrolyzed at 800 °C for 2 h at 10 °C min^{-1} (Fig. 1). The product was thoroughly washed to neutral pH and dried again at 60 °C to obtain the KOH-activated biochar (BC_{KOH}). During high-temperature activation, KOH reacts with the carbon matrix through redox, dehydration, and gasification pathways, generating a highly porous structure and oxygenated surface groups. The overall transformations can be summarized by the following reactions:[24]

$$6KOH + 2C \rightarrow 2K + 3H_2 + 2K_2CO_3$$

$$2K_2CO_3 + C \rightarrow K_2O + CO_2$$

$$K_2CO_3 \rightarrow K_2O + CO_2$$

$$K_2O + C \rightarrow 2K + CO$$

2.4. Preparation of MnO_2-anchored cotton branches KOH-activated biochar (BC_{KOH})

MnO_2 nanoparticles were anchored on BC_{KOH} *via* a modified oxidation-reduction method.[25] Briefly, 1 g of BC_{KOH} was dispersed in 100 mL deionized water using ultrasonication for 1 h. Manganese chloride tetrahydrate (10 mmol) was added and stirred at 80 °C for 1 h, followed by dropwise addition of plant extract with stirring for another hour. Potassium permanganate (50 mmol) was then added, and the mixture was stirred for 6 h at 50 °C.[26] The product was calcined at 500 °C for 2 h (10 °C min^{-1}), collected by centrifugation, washed with deionized water, and dried at 50 °C to yield MnO_2/BC_{KOH}. The overall redox process forming MnO_2 can be represented as follows:[27]

$$3Mn^{2+} + 2MnO_4^- + 2H_2O \rightarrow 5MnO_2(s) + 4H^+$$

2.5. Preparation of $SrSnFe_2O_4$ nanoparticles

Sr–Sn co-doped ferrite nanoparticles were synthesized *via* a green route using cotton branch extract as a bio-reducing and stabilizing agent. $Fe(NO_3)_3 \cdot 9H_2O$, $SnCl_2$, and $SrCl_2 \cdot 6H_2O$ were dissolved in 100 mL of distilled water and stirred for 2 h to ensure complete homogenization. Cotton branch extract was then added dropwise, resulting in a characteristic dark brown colour, confirming nanoparticle nucleation. The mixture was maintained at 90 °C for 2 h, cooled, filtered, and washed repeatedly with distilled water. The obtained powder was dried at 60 °C overnight and subsequently annealed at 500 °C for 2 h to enhance crystallinity. To clarify the reaction pathway, the formation of Sr–Sn co-doped ferrite occurs through phytochemical-assisted oxidation of Sn^{2+} to Sn^{4+}, co-precipitation of mixed metal hydroxides, and solid-state diffusion during annealing, which drives the incorporation of Sr^{2+} and Sn^{4+} into the spinel ferrite lattice. The overall stoichiometric transformation for the target composition $Sr_xSn_xFe_{2-2x}O_4$ ($x = 0.1$) can be summarized by the following simplified solid-state reaction:

$$1.8Fe^{3+} + 0.1Sr^{2+} + 0.1Sn^{4+} + 4O^{2-} \rightarrow Sr_{0.1}Sn_{0.1}Fe_{1.8}O_4$$

2.6. Fabrication of $SrSnFe_2O_4$ decorated MnO_2 anchored BC_{KOH}

$SrSnFe_2O_4$@δ-MnO_2/BC_{KOH} composites were synthesized with varying $SrSnFe_2O_4$ loadings (2–30%) to evaluate their efficiency in removing *ortho*-nitrophenol (*o*-NP) from contaminated water. For each composite, a calculated amount of $SrSnFe_2O_4$ was added to MnO_2/BC_{KOH} and dispersed in 20 mL of distilled water with continuous stirring for 12 h to allow diffusion of the magnetic nanoparticles into the support. The mixture was then sonicated for 1 hour, after which the composite was collected, washed, and dried at 60 °C for 24 hours. The final products were labelled according to their $SrSnFe_2O_4$ content. To clarify the interfacial chemistry occurring during composite formation, the process can be described as involving Fe–O–Mn bridging, partial surface redox events, and electrostatic interactions between positively charged ferrite sites and oxygenated functional groups on δ-MnO_2/BC_{KOH}.

2.7. Materials characterization

Characterization of the materials was performed using various analytical techniques, as detailed in SI Text S2.

2.8. Adsorption study

Ortho-nitrophenol (*o*-NP) was chosen as a model pollutant to evaluate the performance of the $SrSnFe_2O_4$@δ-MnO_2/BC_{KOH} composite. A 1000 mg L^{-1} stock solution was prepared and stored in the dark, with serial dilutions made to obtain concentrations ranging from 50 to 300 mg L^{-1}. Adsorption experiments were conducted in 100 mL conical flasks containing 20 mL of *o*-NP solution, shaken at 300 rpm and 25 °C. The effects of pH (2–10) and composite dosage (5–80 mg) were investigated, and the influence of temperature was assessed using a controlled shaker between 25–55 °C. The residual *o*-NP concentration was measured using a double-beam UV-visible spectrophotometer at 334 nm. The adsorption capacity and the removal efficiency (% *R*) were calculated using the following equations:[28]

$$\% R = \frac{C_0 - C}{C_0} \times 100 \quad (1)$$

$$q = \frac{(C_0 - C) \times V}{m} \quad (2)$$

where C_0 and C are the concentration of the *o*-NP in (mg L^{-1}) at the beginning and a specific time, respectively, V symbolizes the

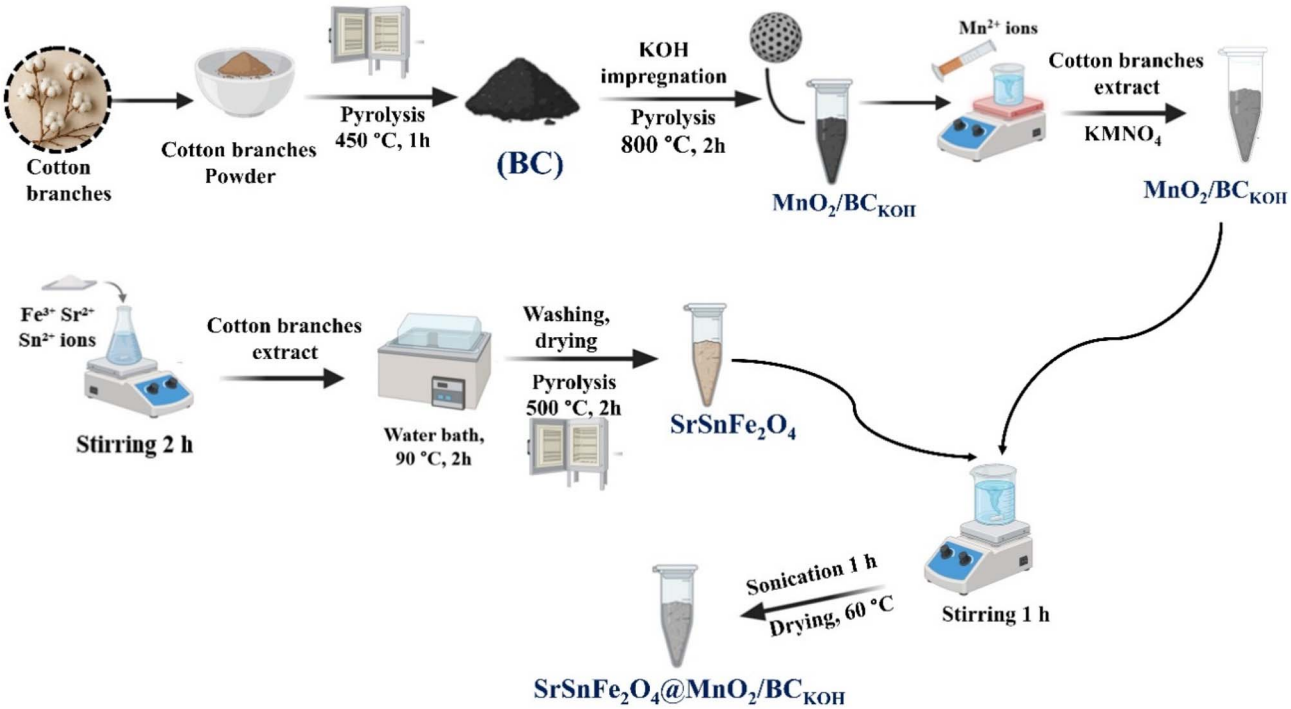

Fig. 1 Schematic illustration of the synthesis pathway of $SrSnFe_2O_4$@δ-MnO_2/BC_{KOH} composite.

o-NP volume in L, and *m* symbolizes $SrSnFe_2O_4$@δ-MnO_2/BC_{KOH} mass in g.

2.9. Interfering ions investigation

The effect of co-existing ions on *o*-NP adsorption by $SrSnFe_2O_4$@δ-MnO_2/BC_{KOH} was investigated using anionic (Cl^-, NO_3^-, SO_4^{2-}, HCO_3^-) and cationic (Na^+, K^+, Ca^{2+}, Mg^{2+}) species. Batch experiments were performed with 0.1 M of each ion, an initial *o*-NP concentration of 50 mg L^{-1}, pH 5, and 0.01 g of adsorbent, shaken at 150 rpm for 1 h to reach equilibrium.

2.10. Regeneration experiment

Desorption was evaluated for $SrSnFe_2O_4$@δ-MnO_2/BC_{KOH} over five consecutive cycles. In each cycle, 0.01 g of the composite was placed in 50 mL of 50 mg L^{-1} *o*-NP solution at pH 5, 25 °C, and shaken at 150 rpm for 1 h. After measuring the residual *o*-NP, the adsorbent was washed with distilled water, dried at 105 °C for 12 h, and subjected to desorption in 50 mL of 0.5 M NaOH or HCl for 2 h at 25 °C. Following desorption, the remaining *o*-NP concentration was recorded, and the adsorbent was washed and dried again at 105 °C for reuse in the next cycle.

2.11. Selectivity study

The selectivity of $SrSnFe_2O_4$@δ-MnO_2/BC_{KOH} was assessed using various pollutants, including *p*-nitrophenol, Congo red, methylene blue, crystal violet, methyl orange, tetracycline, and doxycycline. Batch experiments were conducted at pH 5, with 0.01 g of adsorbent, an initial pollutant concentration of 50 mg L^{-1}, and an equilibrium time of 1 h. Residual concentrations were measured using a double-beam UV-visible spectrophotometer at each compound's maximum wavelength. This study evaluated the composite's ability to remove a diverse range of dyes, antibiotics, and aromatic compounds, highlighting its potential for broad environmental remediation applications.

2.12. Ionic strength study

The effect of ionic strength on the *o*-NP adsorption capacity was evaluated by dissolving a specific amount of NaCl (ranging from 0.2 to 1.0 M) in 20 mL of an *o*-NP solution at pH 6. Next, 0.01 g of the $SrSnFe_2O_4$@δ-MnO_2/BC_{KOH} composite was added to the *o*-NP/NaCl solution, and the mixture was stirred at 150 rpm for 1 hour. After this period, a sample was withdrawn and analyzed to determine the concentration of *o*-NP remaining in solutions.

2.13. Real wastewater sample

Adsorption experiments using real wastewater were conducted by adding 10 mg of $SrSnFe_2O_4$@δ-MnO_2/BC_{KOH} to 25 mL of solutions containing *o*-NP at 10, 30, or 50 mg L^{-1}. The mixtures were maintained at 25 °C, pH 5, and shaken at 180 rpm for 60 min. After adsorption, the solutions were filtered through 0.45 μm PVDF syringe filters, and the filtrates were collected for analysis. All experiments were performed in triplicate, with average values reported.

3. Characterization result and discussion

3.1. FTIR

Fig. 2A shows FTIR spectra for $SrSnFe_2O_4$@δ-MnO_2/BC_{KOH} and its pristine components, as well as raw biomass. The FTIR

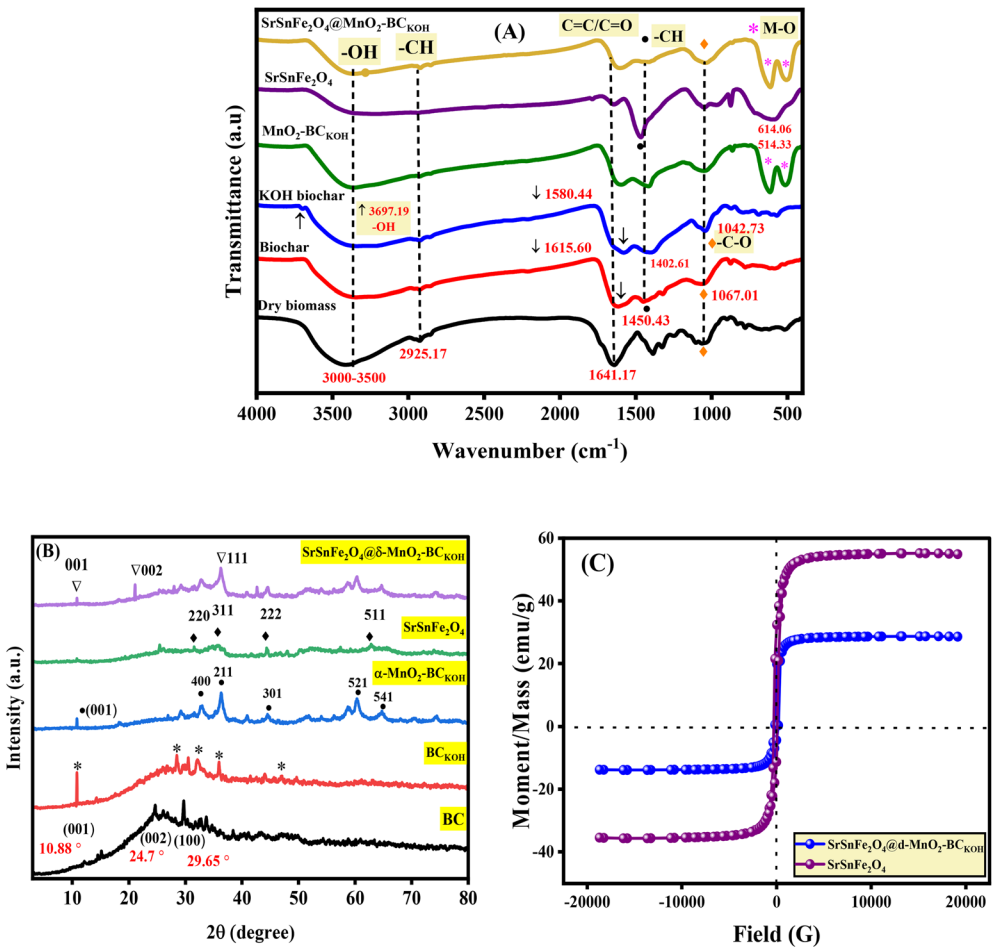

Fig. 2 (A) FTIR spectra and (B) XRD patterns of the $SrSnFe_2O_4$@δ-MnO_2/BC_{KOH} composite and its individual components. (C) VSM magnetization curves of $SrSnFe_2O_4$ and the $SrSnFe_2O_4$@δ-MnO_2/BC_{KOH} composite.

spectrum of the raw biomass exhibits a broad absorption band between 3000–3500 cm^{-1}, indicative of O–H stretching vibrations. The peak at 2925.17 cm^{-1} is associated with C–H stretching in methylene groups, typically present in waxes and fats.[29] The signal at 1450.43 cm^{-1} corresponds to the symmetric bending of CH_2 groups characteristic of both amorphous and crystalline cellulose, and the band at 1067.01 cm^{-1} is attributed to C–O stretching vibrations.[30] Additionally, the peak at 1641.17 cm^{-1} represents carbonyl (C=O) functional groups.[31] For the FTIR spectra of BC and BC_{KOH}, the low-intensity bands in the range of 3000–3500 cm^{-1} correspond to asymmetric and symmetric O–H stretching vibrations on the biochar surface.[32] In BC_{KOH}, a small peak observed at 3679.19 cm^{-1} may indicate the presence of additional hydroxyl groups potentially generated during KOH activation. At the same time, the overall O–H region shows a similar shape and intensity compared with unactivated biochar. These processes enrich the surface with –OH, –COOH, carbonyl, and O–C–O functionalities, consistent with the observed shifts in peak positions and intensities.[33] The bands at 1615.60 cm^{-1} in BC and 1580 cm^{-1} in BC_{KOH} correspond to C=O stretching vibrations,[31] while the peaks at 1450.43 cm^{-1} in BC and 1402.61 cm^{-1} in BC_{KOH} are assigned to C–H bending. Likewise, C–O stretching vibrations are confirmed by the peaks at 1067.01 cm^{-1} in BC and 1042.73 cm^{-1} in BC_{KOH}. These spectral changes collectively confirm that KOH activation substantially alters the surface chemistry by increasing the abundance of polar oxygen-containing functional groups and generating a more reactive surface. The FTIR spectra of MnO_2/BC_{KOH}, $SrSnFe_2O_4$, and the final $SrSnFe_2O_4$@δ-MnO_2/BC_{KOH} composite exhibit two distinct bands at 614.06 and 514.33 cm^{-1}. These peaks correspond to M–O stretching vibrations within octahedral coordination environments, indicating the successful anchoring of MnO_2 nanostructures and the incorporation of $SrSnFe_2O_4$ onto the activated biochar surface.[34]

3.2. XRD analysis

The X-ray diffraction (XRD) patterns of pristine biochar (BC), KOH-activated biochar (BC_{KOH}), α-MnO_2/BC_{KOH}, $SrSnFe_2O_4$, and the $SrSnFe_2O_4$@δ-MnO_2/BC_{KOH} composite are presented in Fig. 2B. The pristine BC exhibited a broad diffraction peak at $2\theta = 24.7°$, indexed to the (002) plane of graphitic carbon, indicating the presence of partially ordered aromatic lamellae. A weaker reflection at $2\theta = 29.65°$ corresponds to the (100) plane of hexagonal carbon domains,[23,35] confirming the turbostratic and nanocrystalline nature of the carbon matrix.[36] The XRD

pattern of BC_{KOH} displayed distinct peaks at $2\theta = 10.77°$, 28.27°, 36.00°, and 46.79°, attributed to trace K_2CO_3 likely remaining after KOH activation and washing. After anchoring α-MnO_2 onto BC_{KOH}, the sample exhibited characteristic reflections of tetragonal α-MnO_2 at 2θ = 32.83° (400), 36.35° (211), 44.56° (301), 60.30° (521), and 64.75° (541), consistent with JCPDS 44-014.[37] The $SrSnFe_2O_4$ ferrite displayed well-defined peaks at 2θ = 31.53°, 35.60°, 44.45°, and 62.75°, assigned to the (220), (311), (222), and (511) crystallographic planes of the cubic spinel phase (JCPDS 82-1042).[38] In the final composite (30% $SrSnFe_2O_4$@δ-MnO_2/BC_{KOH}), distinct modifications in both peak positions and intensities indicate lattice reconstruction and partial transformation of the MnO_2 phase. Notably, new reflections emerged at 2θ = 10.77°, 21.09°, and 36.23°, corresponding to the (001), (002), and (100) planes of birnessite-type δ-MnO_2 (JCPDS 80-1098).[39–41] The low-angle (001) peak around 10.77° associated with an interlayer spacing of ~7 Å is a well-recognized fingerprint of the layered δ-MnO_2 structure, as stated by.[42] Literature reports confirm that the appearance of this basal reflection, combined with the suppression of major α-

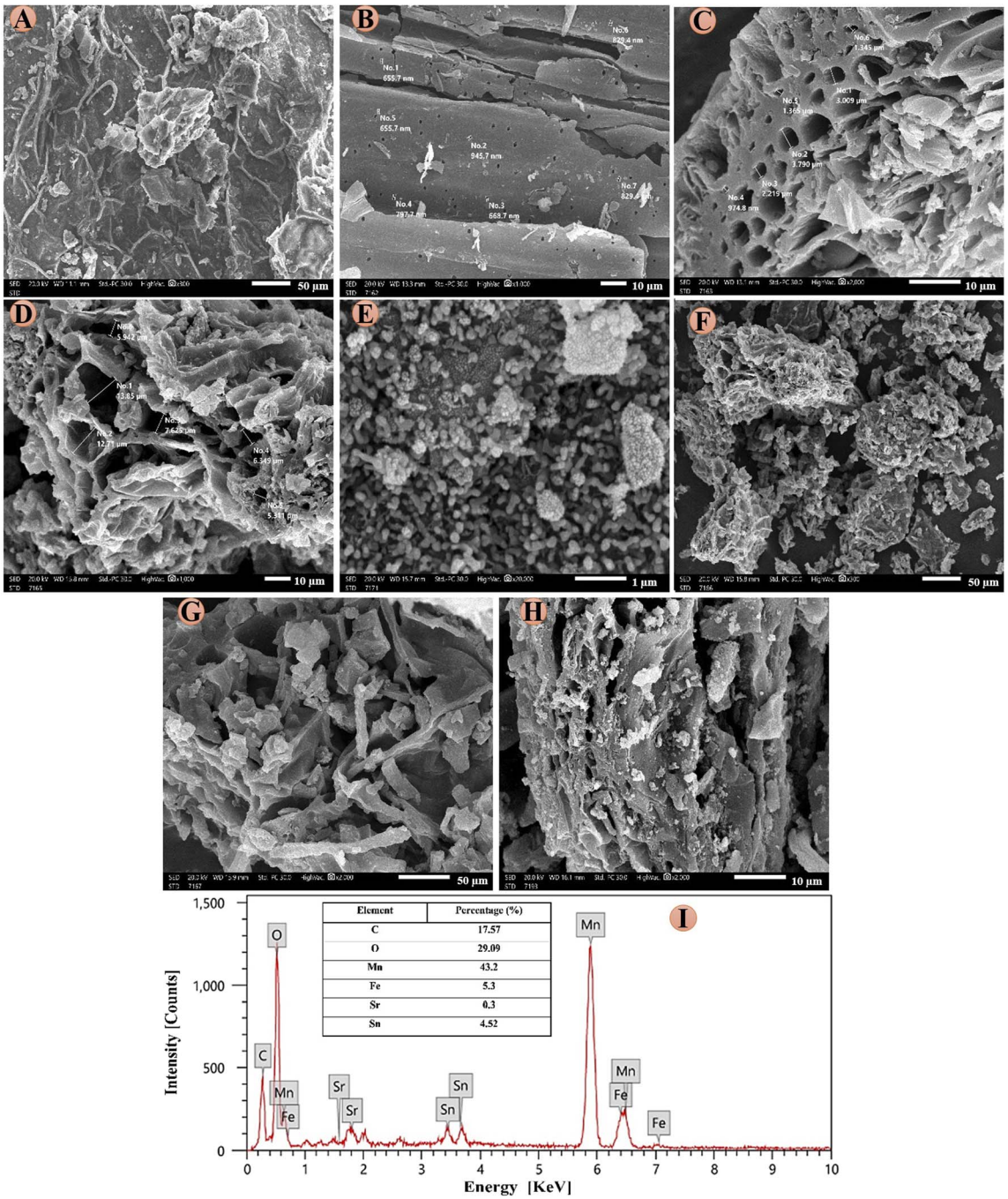

Fig. 3 SEM images of (A) cotton branches dry biomass, (B) pristine BC, (C) KOH activated BC, (D) MnO_2/BC_{KOH}, (E and F) $SrSnFe_2O_4$, and (G and H) $SrSnFe_2O_4$@δ-MnO_2/BC_{KOH} composite. (K) EDX of $SrSnFe_2O_4$@δ-MnO_2/BC_{KOH}.

MnO_2 tunnel-structure peaks, is indicative of an α → δ rearrangement of MnO_6 octahedra during mild synthesis or post-treatment conditions.[43,44]

3.3. VSM analysis

The VSM analysis (Fig. 2C) confirmed that both $SrSnFe_2O_4$ and the $SrSnFe_2O_4$@δ-MnO_2/BC_{KOH} composite exhibit ferrimagnetic behaviour with well-saturated hysteresis loops. Pure $SrSnFe_2O_4$ displayed a coercivity of 205.43 G and a saturation magnetization of 54.87 emu g^{-1}. These values are consistent with predominantly single-domain nanoparticles, as supported by TEM and XRD analyses. Upon incorporation into the δ-MnO_2/BC_{KOH} matrix, the saturation magnetization decreased significantly (M_s = 28.56 emu g^{-1}) due to dilution by the non-magnetic support and weakened interparticle exchange interactions.[45] The reduction in coercivity is associated with lower effective magnetic anisotropy and the dispersion of $SrSnFe_2O_4$ particles within the non-magnetic matrix.[46]

3.4. SEM and EDX analysis

The SEM images (Fig. 3) reveal clear morphological differences among the prepared materials. The raw cotton stalk biomass (Fig. 3A) shows heterogeneous natural textures, with regions ranging from smooth surfaces to rough fibrous structures.[47] The pristine biochar (Fig. 3B) exhibits a relatively smooth and continuous outer surface with a well-defined porous network composed of interconnected channels and multilayered carbon domains, with most pores appearing at the nanoscale. After activation, the KOH-treated biochar (Fig. 3C) displays a strongly developed porous architecture, characterized by enlarged openings and newly formed pores extending into the microscale. Loading MnO_2 onto the activated biochar results in an irregular morphology consisting of fragmented carbon sheets and partially collapsed pore walls, where granular and clustered particles are distributed across the surface and within the pore network (Fig. 3D). The $SrSnFe_2O_4$ particles alone appear as spherical aggregates (Fig. 3E and F). In the final $SrSnFe_2O_4$@δ-MnO_2/BC_{KOH} composite (Fig. 3G and H), ferrite nanoparticles are visibly distributed along the δ-MnO_2/BC_{KOH} surface, forming a continuous heterogeneous coating across the carbon matrix. Elemental mapping *via* EDX (Fig. 3K) shows the presence of C, O, Mn, Sr, Fe, and Sn, consistent with the components of the synthesized composite.

3.5. BET, BJH, and DFT analysis

The N_2 adsorption–desorption isotherms (Fig. 4A and B) exhibit type IV behaviour with H-type hysteresis loops, confirming the

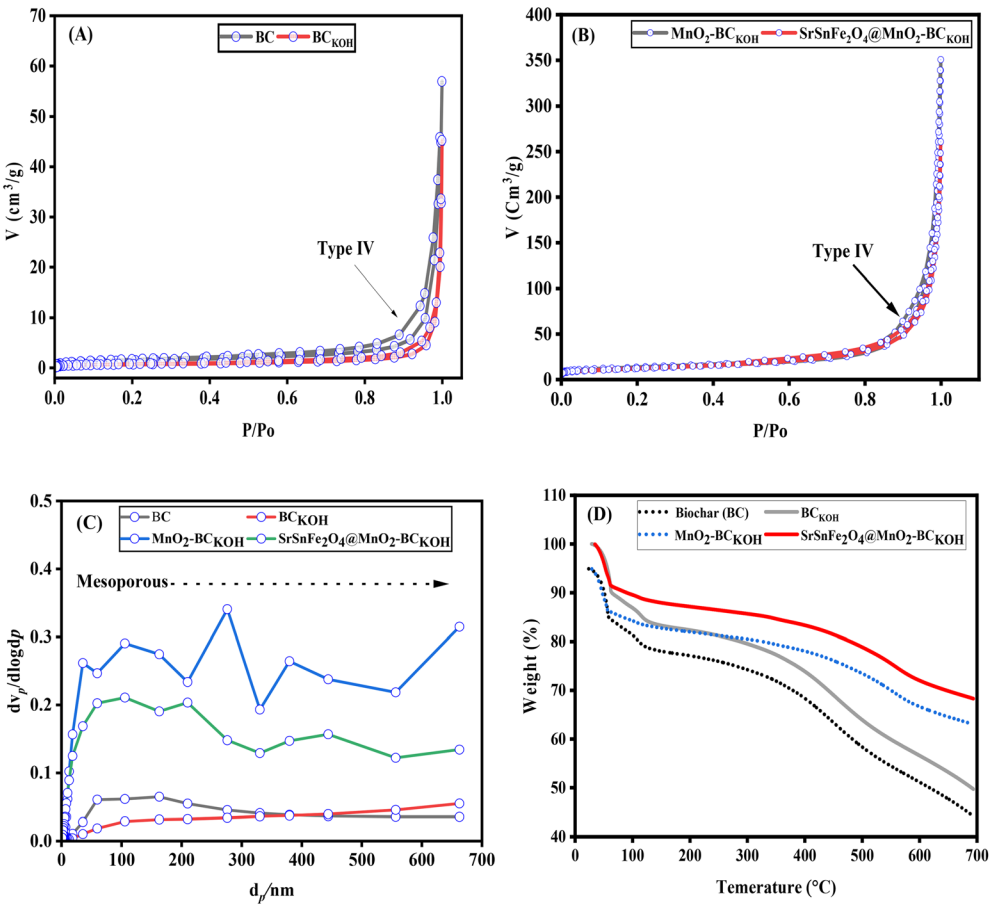

Fig. 4 Nitrogen adsorption–desorption isotherms of (A) BC, and BC_{KOH}, and (B) MnO_2/BC_{KOH} and $SrSnFe_2O_4$@δ-MnO_2/BC_{KOH} composites. (C) BJH pore size distribution curves of all samples. (D) TGA profiles of BC, BC_{KOH}, MnO_2/BC_{KOH}, and $SrSnFe_2O_4$@δ-MnO_2/BC_{KOH} composite.

predominance of mesoporosity and capillary condensation in the prepared materials.[48] BET results (Table 1) show a marked increase in surface area from pristine BC (5.26 m^2 g^{-1}) to BC_{KOH} (57.44 m^2 g^{-1}), followed by a further rise after MnO_2 incorporation (325.02 m^2 g^{-1}), indicating enhanced mesopore development.[9] After introducing 30 wt% $SrSnFe_2O_4$, the surface area decreased to 179.24 m^2 g^{-1}, due to partial pore filling/surface coverage; however, the composite retained a high surface area and an accessible mesoporous network. The BJH/DFT pore size distribution (Fig. 4C) confirms dominant mesopores within 30–47 nm.[49]

Table 1 Textural parameters derived from the BET analysis of the synthesized composite

Adsorbents	Average pore diameter (nm)	S_{BET} (m^2 g^{-1})
BC	32.54	5.26
BC_{KOH}	47.40	57.44
MnO_2@BC_{KOH}	43.8	325.02
$SrSnFe_2O_4$@MnO_2-BC_{KOH}	30.13	179.24

3.6. TGA analysis

Fig. 4D represents the thermal properties of pristine BC, BC_{KOH}, MnO_2-BC_{KOH}, and $SrSnFe_2O_4$@δ-MnO_2/BC_{KOH} composite. The result showed that the combination of BC with KOH, MnO_2, and $SrSnFe_2O_4$ improved the composite thermal stability and weight loss.[50] All samples exhibited initial weight loss below 150 °C, attributed to the release of moisture and volatiles. Pristine BC exhibited continuous degradation, reflecting low thermal stability, while the enhanced thermal stability of BC_{KOH} could be attributed to the formation of more resistant carbon

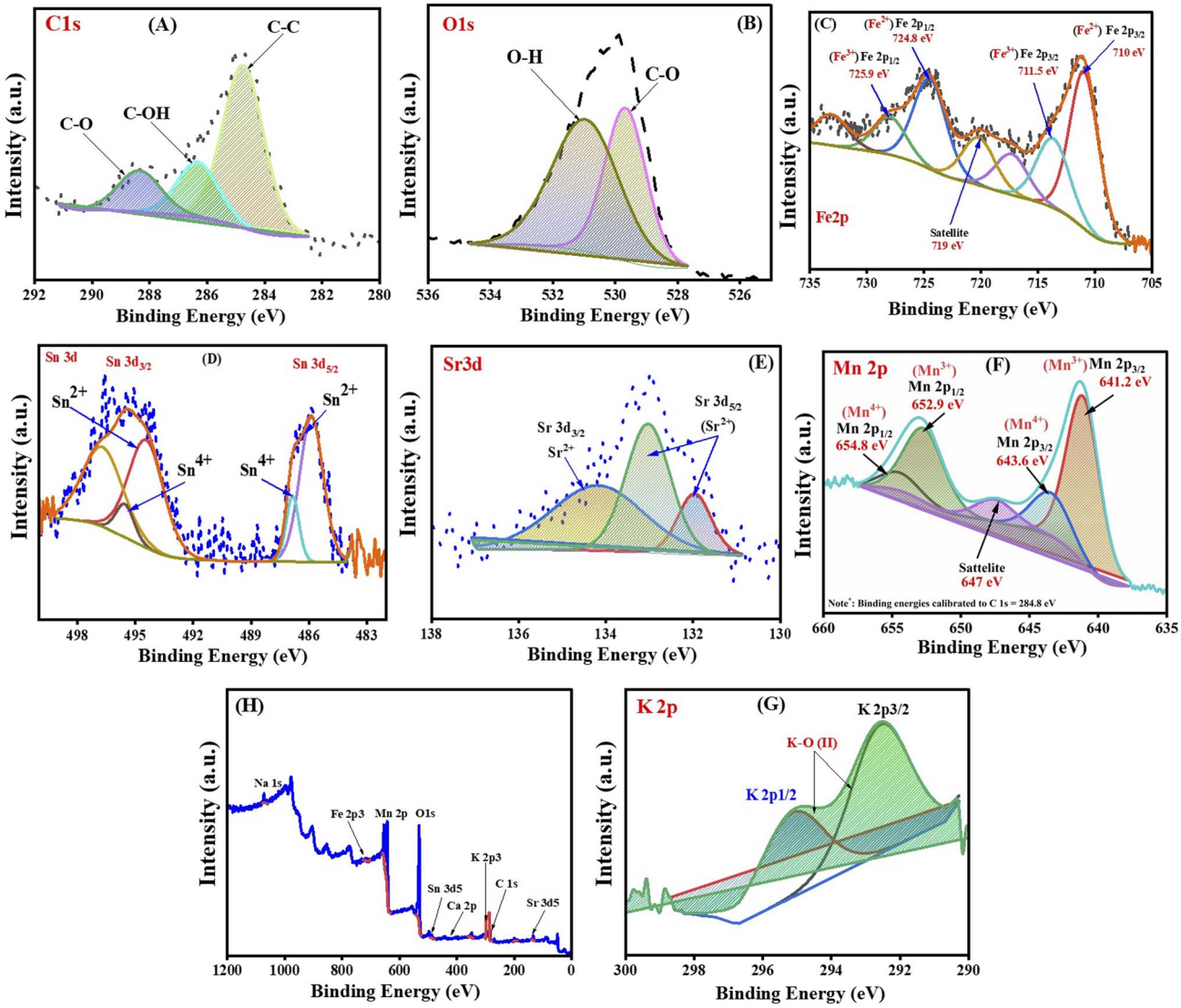

Fig. 5 XPS of 30% $SrSnFe_2O_4$@δ-MnO_2/BC_{KOH} composite, and high-resolution spectra of (A) C 1s, (B) O 1s, (C) Fe 2p, (D) Sn 3d, (E) Sr 3d, (F) Mn 2p, (G) K 2p, (H) survey, and (I) lattice distortion and heterostructure formation.

domains. Further enhancement in stability after MnO_2 incorporation, owing to strong BC-MnO_2 interactions. $SrSnFe_2O_4$@-MnO_2-BC_{KOH} composite retained the highest weight (~69% at 700 °C), demonstrating superior thermal stability due to the synergistic reinforcement of the carbon framework and suppression of pyrolytic degradation,[51] indicating that surface modification and composite formation effectively enhance the structural robustness of biochar.

3.7. XPS analysis

The X-ray photoelectron spectroscopy (XPS) analysis of the $SrSnFe_2O_4$@δ-MnO_2/BC_{KOH} composite is presented in Fig. 5. The C 1s spectrum (Fig. 5A) shows peaks at 284.74, 286.33, and 288.35 eV, corresponding to C–C, C–OH, and C=O groups, confirming oxygenated functionalities on the biochar surface.[52] The O 1s spectrum (Fig. 5B) exhibits peaks at 529.67 eV (lattice oxygen, M–O) and 530.95 eV (surface hydroxyls), reflecting metal–oxygen interactions.[53] The Fe 2p spectrum (Fig. 5C) indicates the coexistence of Fe^{2+} and Fe^{3+} states, with Fe^{2+} $2p_{3/2}$ and $2p_{1/2}$ at 709.5 and 724.8 eV, and Fe^{3+} $2p_{3/2}$ and $2p_{1/2}$ at 711.3 and 725.9 eV, together with characteristic satellite features at ~719 eV, confirming mixed-valence iron in the ferrite lattice.[54] The Mn 2p spectrum (Fig. 5F) reveals Mn^{3+} and Mn^{4+} species, with Mn^{3+} $2p_{3/2}$ and $2p_{1/2}$ at 641.2 and 652.9 eV, and Mn^{4+} $2p_{3/2}$ and $2p_{1/2}$ at 643.6 and 654.8 eV, along with a satellite at 647 eV, supporting correct oxidation-state assignment.[55] The Sn 3d spectrum (Fig. 5D) confirmed mixed Sn^{2+}/Sn^{4+} oxidation states, with Sn^{4+} $3d_{5/2}$ and $3d_{3/2}$ peaks at 486.85 and 495.56 eV, and Sn^{2+} at 485.87 and 494.34 eV. Moreover, a weak Sn satellite structure appeared at (~492–493 eV), ensuring fitting accuracy.[56] The Sr 3d spectrum (Fig. 5E) displayed Sr $3d_{5/2}$ and $3d_{3/2}$ peaks at 131.97 and 133.06 eV, along with a higher-energy shake-up component at 134.18 eV, confirming Sr incorporation in an oxidized environment.[57] Residual K 2p peaks at 292.55 and 295.02 eV reflect the presence of potassium from the KOH activation step.[58] The survey spectrum (Fig. 5H) confirms the presence of all intended elements (Fe, Sn, Sr, Mn, O, C, K), indicating successful composite fabrication. To ensure accurate oxidation-state identification, all XPS spectra were refitted using appropriate constraints for spin–orbit splitting, fixed doublet area ratios, and consistent FWHM values. Satellite features for Fe, Mn, Sr, and Sn were included, and detailed fitting parameters are provided in the SI (Table S1).

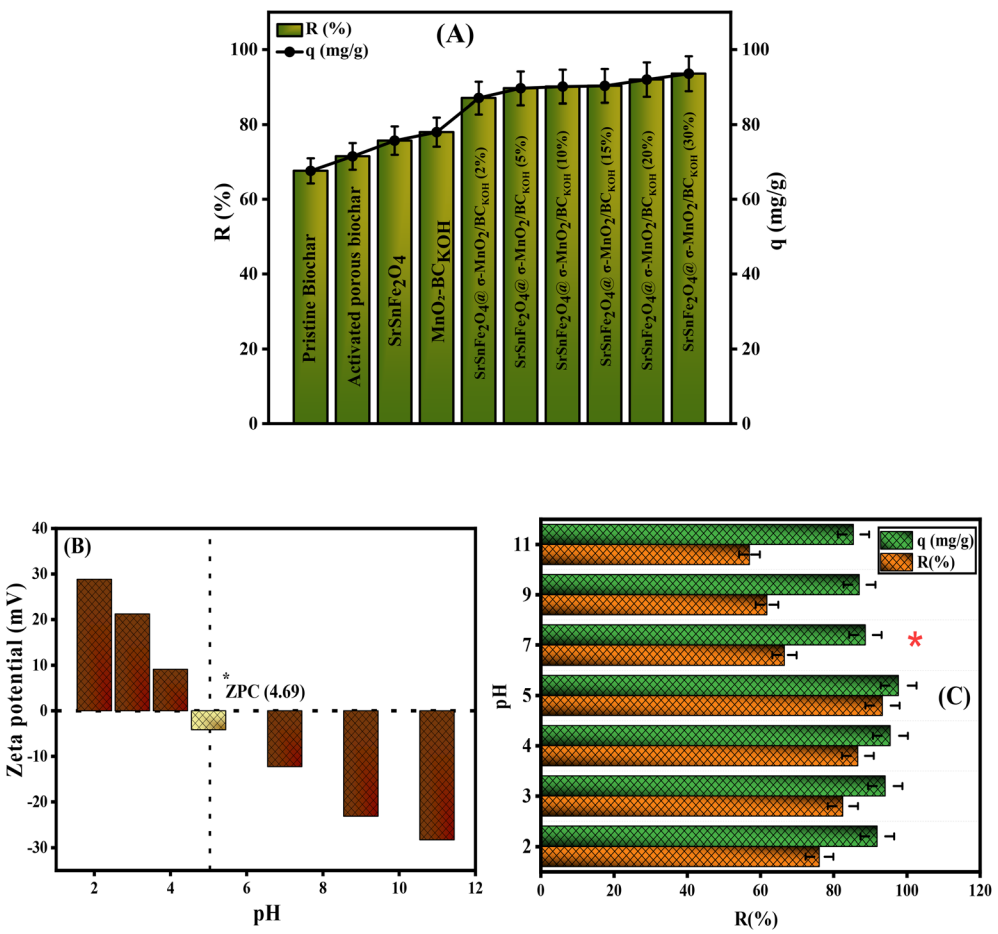

Fig. 6 (A) Comparative adsorption study of *o*-nitrophenol (*o*-NP) [pH = 5, C_0 = 50 mg L^{-1}, m = 0.01 g, T = 25 °C]. (B) Point of zero charge (pH_pzc) of the $SrSnFe_2O_4$@δ-MnO_2/BC_{KOH} composite. (C) Effect of solution pH on the adsorption of *o*-NP [C_0 = 50 mg L^{-1}, m = 0.01 g, T = 25 °C].

4. The performance of $SrSnFe_2O_4$@δ-MnO_2/BC_{KOH} composite

4.1. Comparison test

To evaluate the adsorption performance of individual components before integrating them into the composite, a comparative study was conducted. This study examined pristine BC, BC_{KOH}, $SrSnFe_2O_4$, and MnO_2/BC_{KOH}, along with five $SrSnFe_2O_4$@δ-MnO_2/BC_{KOH} composites containing different ferrite loading percentages (2–30%), as shown in Fig. 6A. The removal %, and q (mg g^{-1}) of pristine BC, BC_{KOH}, $SrSnFe_2O_4$, and MnO_2/BC_{KOH} were found to be 56.98% and 85.41 mg g^{-1}, 61.76% and 87.03 mg g^{-1}, 66.54% and 88.65 mg g^{-1}, 71.32% and 90.28 mg g^{-1}, respectively. As ferrite loading increased from 2 to 30 wt%, the removal % and capacity increased from 80.88% and 93.52 mg g^{-1} to 93.31% and 97.73 mg g^{-1}. These findings indicate that modifying MnO_2/BC_{KOH} with $SrSnFe_2O_4$ significantly improves adsorption capacity and removal efficiency, reflecting increases in surface area and active sites. Given its superior adsorption performance, the $SrSnFe_2O_4$@δ-MnO_2/BC_{KOH} composite with 30% ferrite loading was selected for subsequent batch adsorption experiments.

4.2. Effect of pH

The point of zero charge (pH_{ZPC}) is a key parameter governing surface charge behaviour and adsorption performance. The pH_{ZPC} of the $SrSnFe_2O_4$@δ-MnO_2/BC_{KOH} composite was determined from zeta potential measurements to be 4.69 (Fig. 6B). At pH values below 4.69, surface protonation dominates, resulting in a positively charged surface. In contrast, deprotonation occurs at higher pH values, yielding a negatively charged surface. The effect of solution pH on *o*-NP adsorption is presented in Fig. 6C. Maximum adsorption was achieved at pH 5. In contrast, adsorption efficiency declined under both strongly acidic (pH 2–4) and neutral-to-alkaline conditions (pH 7–11). At pH < 4.69, excessive protonation leads to competitive occupation of surface functional groups by H^+ ions, reducing the availability of active sites for *o*-NP adsorption. This decrease could be attributed to site competition rather than material instability. At pH values above the pK_a of *o*-NP (7.23), *o*-NP molecules become deprotonated and negatively charged. Since the composite surface is also negatively charged above its pH_{ZPC}, electrostatic repulsion significantly suppresses adsorption. Under mildly acidic conditions (pH ≈ 5), where *o*-NP remains predominantly in its neutral form, adsorption is

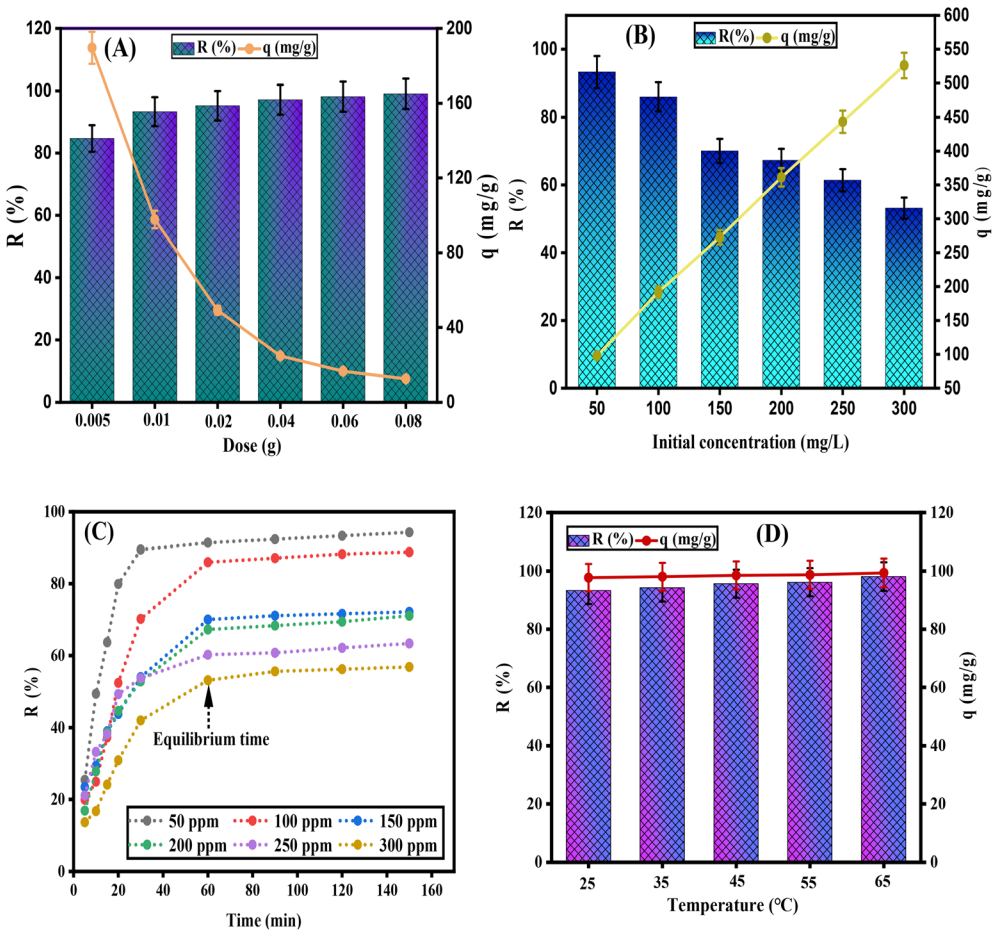

Fig. 7 (A) Effect of adsorbent dosage on the adsorption of *o*-nitrophenol (*o*-NP) [C_0 = 50 mg L^{-1}, pH 5, 25 °C], (B) effect of initial *o*-NP concentration on adsorption performance [*m* = 0.01 g, pH 5, 25 °C], (C) effect of contact time on *o*-NP adsorption [C_0 = 50–300 mg L^{-1}, *m* = 0.01 g, 25 °C, pH 5], (D) effect of temperature on the adsorption of *o*-NP [pH 5, *m* = 0.01 g, C_0 = 50 mg L^{-1}].

governed by non-electrostatic interactions, including π–π stacking, hydrogen bonding, and electron donor–acceptor interactions between *o*-NP and the oxygen-rich carbon matrix and metal oxide surfaces of the composite.

4.3. Dose effect

Fig. 7A shows that increasing the $SrSnFe_2O_4$@δ-MnO_2/BC_{KOH} dosage from 0.005 to 0.08 g improved the *o*-NP removal efficiency (from 84.70% to 99.04%) due to the greater number of available adsorption sites. In contrast, the adsorption capacity decreased (from 189.63 to 12.46 mg g^{-1}) with increasing dosage. This commonly observed effect results from site overlapping and particle aggregation at higher solid concentrations, which reduces the effective surface area per gram and leaves a larger fraction of active sites unsaturated.[59]

4.4. Initial concentration effect

As shown in Fig. 7B, increasing the initial *o*-NP concentration from 50 to 300 mg L^{-1} reduced the $SrSnFe_2O_4$@δ-MnO_2/BC_{KOH} removal efficiency from 93.31% to 53.11%. This decline is attributed to the limited number of active sites on $SrSnFe_2O_4$@δ-MnO_2/BC_{KOH}, which become saturated at higher pollutant concentrations, leaving excess *o*-NP unadsorbed.[60] In contrast, the adsorption capacity increased markedly from 97.73 mg g^{-1} to 526.09 mg g^{-1}, driven by the stronger concentration gradient at elevated *o*-NP levels. This gradient enhances mass transfer, overcomes ion diffusion resistance, and facilitates adsorption onto available sites. Thus, optimizing both initial concentration and adsorbent dosage is essential for practical applications.[61] Notably, the $SrSnFe_2O_4$@δ-MnO_2/BC_{KOH} composite achieved rapid adsorption, reaching equilibrium within 60 min (Fig. 7C).

4.5. Temperature effect

The adsorption of *o*-NP onto $SrSnFe_2O_4$@δ-MnO_2/BC_{KOH} was confirmed to be an endothermic process, as the removal efficiency increased from 93.52% to 98.96% when the temperature rose from 25 °C to 65 °C, with a corresponding rise in adsorption capacity from 97.73 to 99.35 mg g^{-1} (Fig. 7D). This enhancement can be attributed to three factors: (1) elevated temperatures increase molecular motion and collision frequency with the adsorbent, promoting adsorption; (2) according to the Arrhenius equation, heat supplies the activation energy required for adsorption; and (3) thermal swelling of the adsorbent generates additional porosity, facilitating access to internal active sites.[62] Nevertheless, given the cost-effectiveness and operational simplicity, adsorption isotherm studies were conducted at ambient temperature, despite optimal performance at 65 °C.

4.6. Kinetic study

The adsorption of *o*-NP onto $SrSnFe_2O_4$@δ-MnO_2/BC_{KOH} was found to proceed through multiple mechanisms, influenced by surface heterogeneity and physicochemical conditions. To analyse the process kinetics, pseudo-first-order (PFO) (Fig. 8A), pseudo-second-order (PSO) (Fig. 8B), and Elovich (Fig. S1) models have been examined. The linearized forms of these models are listed in Table S2. Based on R^2 values (Table 2), the PSO model provided the best fit ($R^2 \approx 1$), with predicted adsorption capacities (q_{cal}) closely matching the experimental results (q_{exp}), confirming its suitability for describing the adsorption process. The Elovich model parameters further support the presence of a heterogeneous adsorption surface, where α represents the initial adsorption rate, and β reflects the gradual decrease in adsorption energy as surface sites become progressively occupied. The high α value suggests rapid initial uptake, whereas the β value indicates surface energetic heterogeneity rather than an actual desorption rate.[63]

4.7. Isotherm study

To assess the adsorption behaviour of *o*-NP, four isotherm models, Langmuir, Freundlich, Temkin, and Dubinin–Radushkevich (D–R) were applied. The linear fits (Fig. 9) and derived parameters (Table S3) show that the Freundlich model provides the best description of the experimental data (R^2 = 0.985), outperforming the Langmuir (R^2 = 0.910), Temkin (R^2 =

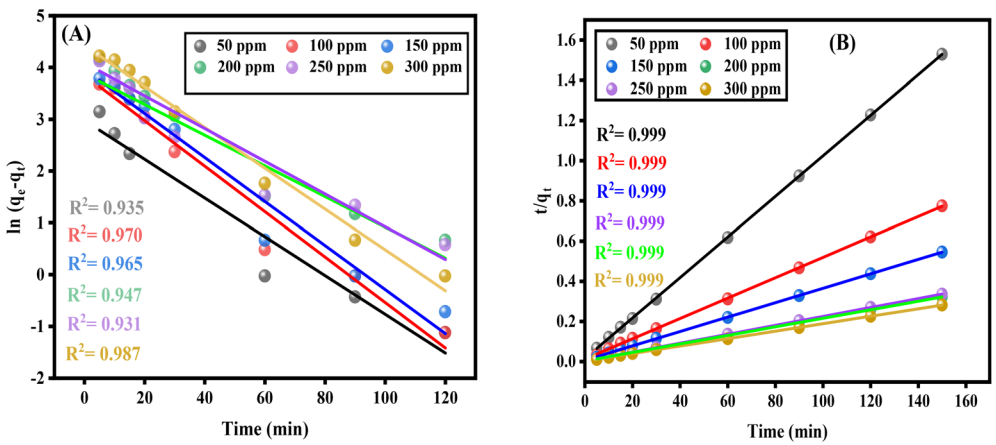

Fig. 8 Kinetics models: (A) pseudo-first order, (B) pseudo-second order for *o*-NP adsorption by $SrSnFe_2O_4$@δ-MnO_2/BC_{KOH}.

Table 2 Kinetic parameters of the *o*-NP adsorption $SrSnFe_2O_4$@δ-MnO_2/BC_{KOH}

	o-NP initial concentration (mg L^{-1})					
Model parameters	50	100	150	200	250	300
Experimental, q_e (mg g^{-1})	97.73	193.51	274.71	365.64	446.19	531.29
Pseudo-first order (PFO)						
Calculated, q_e (mg g^{-1})	9.67	47.14	52.78	68.09	53.18	92.17
k_1 (min^{-1})	0.031	0.043	0.042	0.0051	0.033	0.001
R^2	0.935	0.970	0.965	0.947	0.931	0.987
PSO						
Calculated, q_e (mg g^{-1})	99.09	196.89	278.83	369.63	449.09	537.42
k_2 (mg g^{-1})	0.0069	0.0022	0.0020	0.0015	0.0014	0.0012
R^2	0.999	0.999	0.999	0.999	0.999	0.999
Elovich						
α (mg g^{-1} min^{-1})	3.67×10^5		2.15×10^5	1.79×10^7	1.08×10^{10}	2.01×10^9
β (g mg^{-1})	0.157	0.074	0.068	0.05	0.045	0.043
R^2	0.823	0.933	0.960	0.965	0.922	0.955

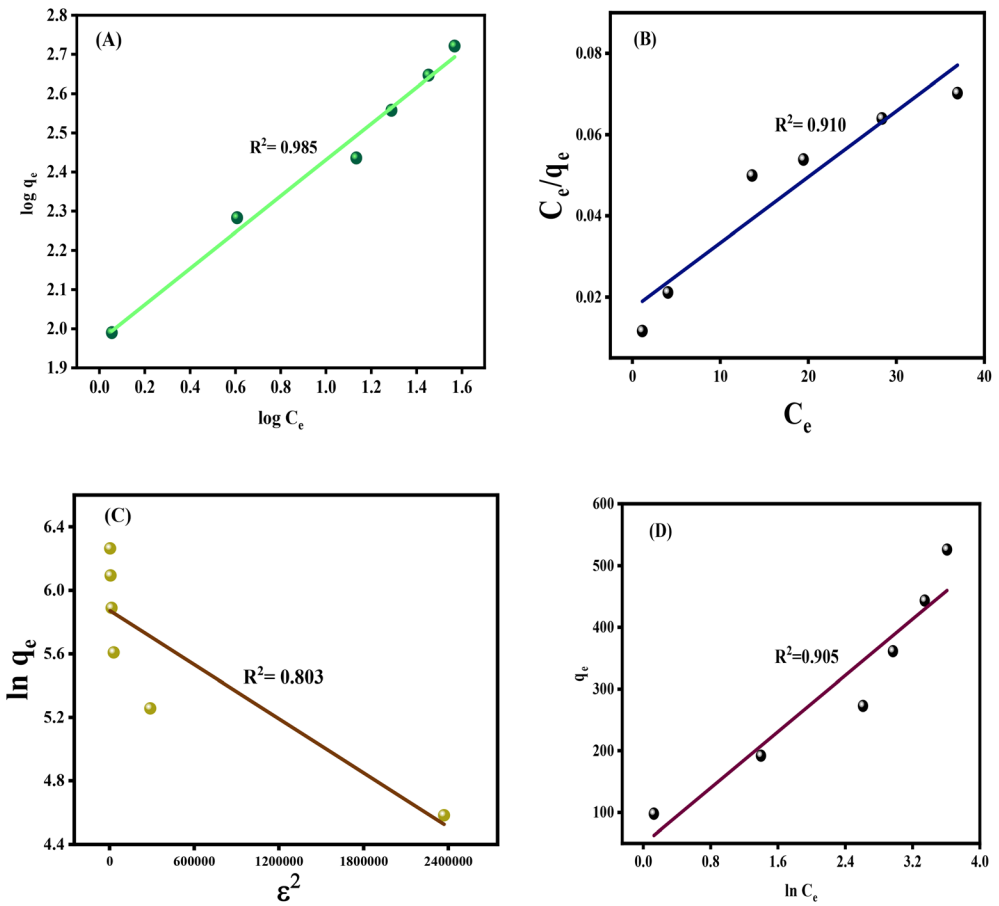

Fig. 9 Linear fitting plots of (A) Freundlich, (B) Langmuir, (C) D–R, and (D) Temkin isotherm models to the adsorption data of *o*-NP onto $SrSnFe_2O_4$@δ-MnO_2/BC_{KOH} composite.

0.905), and D–R (R^2 = 0.803) models (Table 3). The Langmuir model yielded a maximum monolayer adsorption capacity (q_{max}) of 525.51 mg g^{-1}. The Freundlich constant (n > 2) indicates highly favourable adsorption on a heterogeneous surface, consistent with the composite's engineered porosity. The Temkin constant (b < 80 kJ mol^{-1}) and the D–R mean adsorption energy (E < 8 kJ mol^{-1}) suggest that physisorption is a main part of the process.[64]

Table 3 Values of the isotherm parameters for the adsorption of *o*-NP onto $SrSnFe_2O_4$@δ-MnO_2/BC_{KOH} composite

Isotherm model	Parameter	Value
Langmuir	[q_{max} (mg g^{-1})]	525.51
	[b (L mg^{-1})]	0.835
	(R_L)	0.0097
	(R^2)	0.910
Freundlich	[K_F (L mg^{-1})]	7.162
	(n)	2.164
	(R^2)	0.985
Temkin	[B (J mol^{-1})]	21.746
	[b (kJ mol^{-1})]	0.022
	(A)	1.531
	(R^2)	0.905
D–R	q_s (mg g^{-1})	355.467
	K_{ad} (mol^{-2} $k^{-2}J^{-2}$)	51.850
	E (kJ mol^{-1})	0.098
	R^2	0.803

4.8. Thermodynamics study

The thermodynamic behaviour of *o*-NP adsorption onto $SrSnFe_2O_4$@δ-MnO_2/BC_{KOH} was assessed by calculating the standard enthalpy change (ΔH^0, kJ mol^{-1}), Gibbs free energy change (ΔG^0, kJ mol^{-1}), and entropy change (ΔS^0, J K^{-1} mol^{-1}), using the equations provided in Table S4. The thermodynamic parameters derived from the van't Hoff plot (Fig. S2) are listed in Table 4, indicating that the adsorption process is endothermic, as evidenced by the positive ΔH. The negative ΔG values confirm that the adsorption process is spontaneous. Additionally, the positive ΔS value implies increased randomness at the solid–liquid interface, indicating that the migration of *o*-NP ions into the adsorbent structure is accompanied by an increase in disorder.[7]

4.9. Ionic strength effect

Fig. 10A illustrates the effect of ionic strength on the adsorption of *o*-NP onto the $SrSnFe_2O_4$@δ-MnO_2/BC_{KOH} composite. Increasing the NaCl concentration from 0.2 to 1.0 M improved adsorption performance, with the removal efficiency rising from 93.31% to 98.01% and the adsorption capacity increasing from 97.73 to 99.35 mg g^{-1}. This enhancement is likely due to the salting-out effect, wherein dissolved ions disrupt the structured network of water molecules. This disruption reduces the available cavities for accommodating *o*-NP, leading to decreased pollutant solubility and, consequently, enhanced adsorption onto the composite.[65]

4.10. Interfering ions effect

Real water systems often contain multiple contaminants that can compete with target pollutants for adsorption sites. To assess this effect, batch experiments were performed to evaluate the influence of common co-existing ions on the adsorption of *o*-NP by $SrSnFe_2O_4$@δ-MnO_2/BC_{KOH}. As shown in Fig. 10B and C, the presence of both anions (Cl^-, NO_3^-, SO_4^{2-}, HCO_3^-) and cations (Na^+, K^+, Ca^{2+}, Mg^{2+}) caused varying degrees of inhibition. Monovalent cations (Na^+, K^+) led to only minor reductions in removal efficiency (~10.7%). In contrast, divalent cations (Ca^{2+}, Mg^{2+}) produced a more substantial effect (~23.9%), attributed to their higher charge density and stronger electrostatic interactions with the adsorbent surface. Similarly, monovalent anions (Cl^-, NO_3^-, HCO_3^-) reduced efficiency by ~24%, while multivalent anions decreased it further to ~32.5%. Overall, these results indicate that co-existing ions moderately influence adsorption performance, with multivalent species exerting the most significant interference. Notably, despite these competitive effects, $SrSnFe_2O_4$@δ-MnO_2/BC_{KOH} maintained strong adsorption capacity, demonstrating its robustness and potential for practical wastewater treatment in complex real-world systems.[66]

4.11. Reusability study

Regeneration is a crucial characteristic of these composites, reflecting their stability and contributing to cost reduction through high reuse efficiency. As shown in Fig. 10D, the regeneration experiment demonstrated that the $SrSnFe_2O_4$@δ-MnO_2/BC_{KOH} composite maintained impressive performance, with only a 49.71% decrease in removal efficiency and a 83.14 mg g^{-1} reduction in adsorption capacity after five consecutive cycles. This favourable outcome is attributed to the durability of the synthesized composite and its excellent separation efficiency (Fig. 10D), which minimizes mass loss during recovery. The observed decline in removal efficiency over successive cycles may be due to partial pore blockage within the composite, reducing the availability of active adsorption sites.[67]

5. Proposed mechanism of *o*-NP adsorption onto $SrSnFe_2O_4$@δ-MnO_2/BC_{KOH}

Kinetic, isotherm, and thermodynamic analyses indicated that *o*-NP adsorption onto $SrSnFe_2$ O_4@δ-MnO_2/BC_{KOH} involves both physical and chemical interactions. To further elucidate these processes, XPS analysis of the composite after *o*-NP uptake was conducted (Fig. 11). The survey spectrum (Fig. 11A) revealed apparent shifts in core-level binding energies, confirming strong surface interactions between *o*-NP molecules and the composite. Specifically, the Fe 2p peak shifted to lower energy (706.52 eV). In comparison, the Sn 3d peak shifted to higher

Table 4 Thermodynamic parameters of *o*-NP removal onto $SrSnFe_2O_4$@δ-MnO_2/BC_{KOH} composite

Thermodynamic parameters	ΔG^0 (kJ mol^{-1})					ΔH^0 (kJ mol^{-1})	ΔS^0 (J K^{-1} mol^{-1})
Temperature (K)	298	308	318	328	338	24.37	117.98
	−10.78	−11.96	−13.14	−14.32	−15.50		

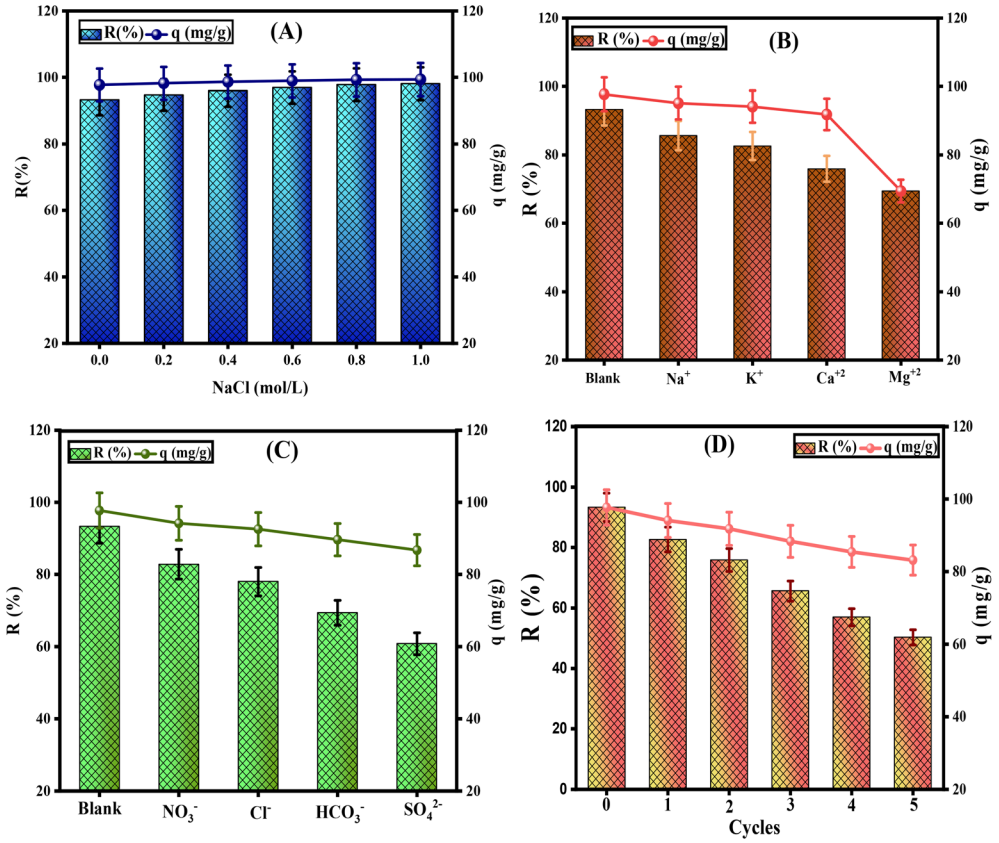

Fig. 10 (A) Effect of ionic strength of *o*-NP adsorption onto $SrSnFe_2O_4$@δ-MnO_2/BC_{KOH} composite. [NaCl = 0.2–1.0 mol L^{-1}, C_0 = 50 mg L^{-1}, pH = 5, and m = 0.01 g]. (B and C) Effect of interfering\ions on *o*-NP adsorption [ions concentration = 0.1 mol L^{-1}, C_0 = 50 mg L^{-1}, pH = 5, and m = 0.01 g]. (D) Regeneration of $SrSnFe_2O_4$@δ-MnO_2/BC_{KOH} [C_0 = 50 mg L^{-1}, pH = 5, and m = 0.01 g].

energy (496.53 eV), and a decrease in Mn 2p intensity indicated coordination between Mn sites and *o*-nitrophenol functional groups. High-resolution spectra of Fe 2p, Mn 2p, Sn 3d, and Sr 3d (Fig. 11D–G) further supported these interactions, showing energy shifts and attenuation of characteristic peaks (*e.g.*, Mn 2p at 674.69 eV). Notably, the Sn 3d peak shifted from 495.5 to 496.89 eV and the Sr 3d peak from 131.98 to 133.68 eV, suggesting metal-ligand coordination with *o*-NP. Shifts in the C–O and O–C=O peaks indicate additional contributions from hydrogen bonding, electrostatic attraction, π–π donor–acceptor interactions, and partial covalent character. The adsorption mechanism is further influenced by solution pH. The point of zero charge (pH_{PZC}) of the composite, determined by zeta potential measurements, is 4.69 (Fig. 6B). At pH values below 4.69, the surface is positively charged due to protonation. In contrast, at pH values above 4.69, deprotonation renders the surface negatively charged. Maximum *o*-NP adsorption occurs at pH 5, where *o*-NP remains predominantly neutral and electrostatic repulsion is minimal. Under strongly acidic conditions (pH 2–4), excessive protonation leads to competition between H^+ ions and *o*-NP molecules for adsorption sites, reducing uptake. At pH values above the pK_a of *o*-NP (7.23), *o*-NP becomes negatively charged, and adsorption is suppressed due to electrostatic repulsion from the negatively charged composite surface. Overall, *o*-NP adsorption onto $SrSnFe_2O_4$@δ-MnO_2/BC_{KOH} proceeds *via* a multi-pathway mechanism. Physical interactions, such as pore filling, van der Waals forces, and π–π stacking between *o*-NP molecules and aromatic rings of the biochar, contribute to adsorption, while chemical interactions occur through surface complexation between the –OH and –NO_2 groups of *o*-NP and surface metal centres (Fe^{3+}, Sn^{4+}, Mn^{4+}), forming inner-sphere complexes. In addition, pH-mediated effects, including surface charge modulation and protonation/deprotonation of functional groups, govern electrostatic attraction or repulsion, influencing overall adsorption efficiency. These synergistic interactions among the composite's functional groups, metal sites, and solution pH enhance the adsorption efficiency of *o*-NP. Fig. 12 illustrates the main pathways and interactions responsible for *o*-NP uptake onto $SrSnFe_2O_4$@δ-MnO_2/BC_{KOH}.

5.1. Selective adsorption study for different pollutants

Investigating adsorption selectivity is critical for assessing the performance of $SrSnFe_2O_4$@δ-MnO_2/BC_{KOH} toward different classes of pollutants. As shown in Fig. 13A, the composite exhibited variable but high removal efficiencies and adsorption capacities for antibiotics, dyes, and nitrophenol isomers. For antibiotics, removal reached 66.48 and 69.78 mg g^{-1} for doxycycline and tetracycline, respectively. For dyes, Congo red

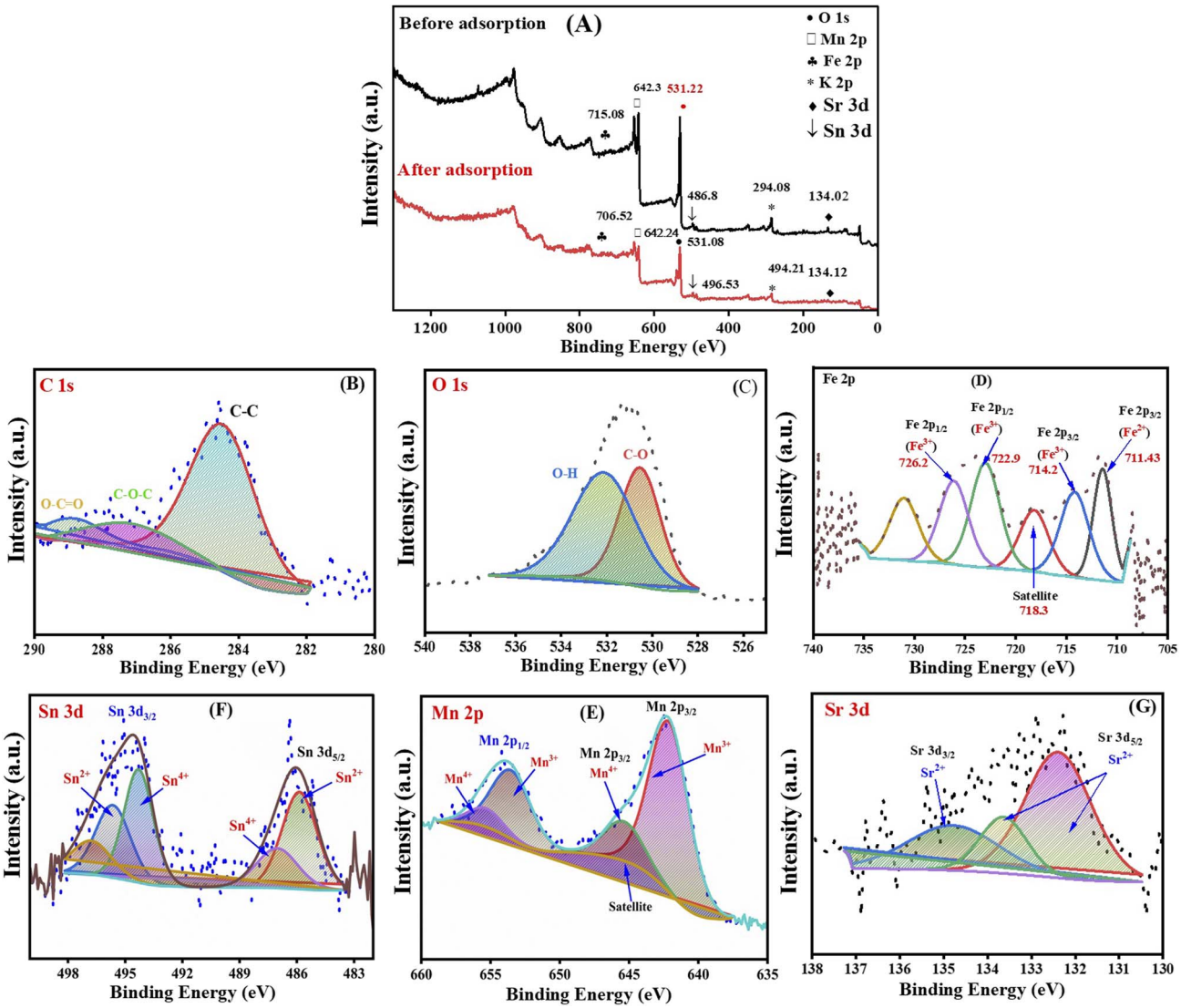

Fig. 11 XPS of $SrSnFe_2O_4$@δ-MnO_2/BC_{KOH} composite after *o*-NP removal; (A) survey, (B) C 1s, (C) O 1s, (D) Fe 2p, (E) Mn 2p, (F) Sn 3d, and (G) Sr 3d.

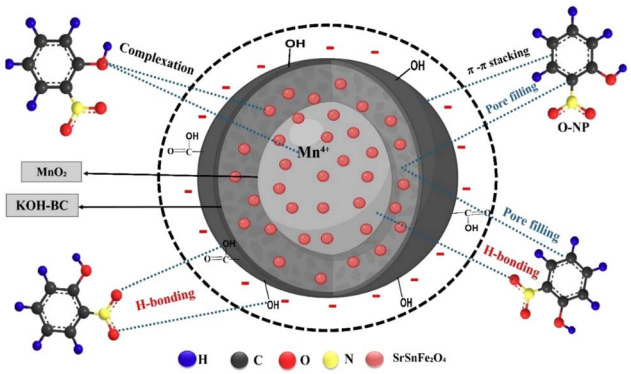

Fig. 12 Plausible adsorption mechanism for the removal of *o*-NP on $SrSnFe_2O_4$@δ-MnO_2/BC_{KOH} composite.

(anionic) and methylene blue, the capacities reached 62.14 and 72.84 mg g^{-1}, respectively, indicating a variety of interactions with the surface-active sites. Notably, superior performance was achieved for *m*-nitrophenol and *p*-nitrophenol with removal capacities of 81.82 and 89.65 mg g^{-1}, respectively.

5.2. Real wastewater sample experiment

A 25 mL real wastewater sample was spiked with *o*-NP at three initial concentrations (10, 30, and 50 mg L^{-1}) using standardized stock solutions. In addition, a synthetic *o*-NP mixture was prepared and used for method optimization and removal evaluation. The developed procedure, optimized using known concentrations, was subsequently applied to real wastewater to assess practical performance. The removal efficiencies in real wastewater were 85.75%, 74.21%, and 68.54% at initial *o*-NP concentrations of 10, 30, and 50 mg L^{-1}, respectively (Fig. 13B). The lower removal at higher concentrations is attributed to

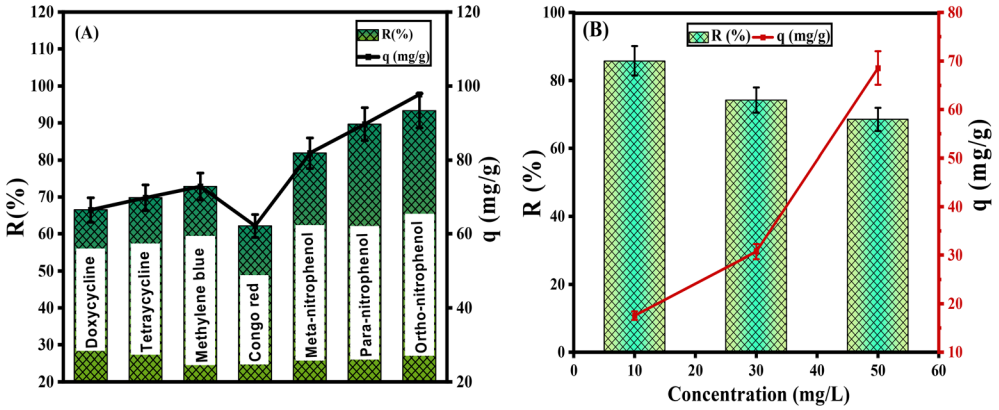

Fig. 13 (A) Selectivity study for the adsorption of various pollutants onto $SrSnFe_2O_4$@δ-MnO_2/BC_{KOH}, (B) adsorption performance of $SrSnFe_2O_4$@δ-MnO_2/BC_{KOH} for *o*-NP removal from real water samples.

Table 5 Comparison between the capacity of $SrSnFe_2O_4$@δ-MnO_2/BC_{KOH} composite and reported adsorbents for the removal of nitrophenols

Adsorbent	Q (mg g^{-1})	pH	Ref.
Waste rubber-derived porous carbon (WRPC)	393.42	6	68
Pine sawdust biochar	117.16	6	69
Ball-milled biochar-vermiculite/zeolite magnetic composites	196.14	6	70
Date seed-based biochar	43.19	7	71
Mg-activation on sugarcane bagasse biochar	144.93	7	72
Cu & Ni-impregnated MnO_2/s-doped biochar	75.76	4	73
Pickling-reheating activated alfalfa biochar	117.65	5	74
EDTA-4Na- and KOH-modified almond shell biochar	149	2	75
Lignin-based KOH-activated carbon	612	7.2	61
Activated sunflower stem biochar	333	2	24
$SrSnFe_2O_4$@δ-MnO_2/BC_{KOH}	525.51	5	Current study

progressive saturation of available adsorption sites. Moreover, the slightly reduced performance in real wastewater compared to spiked samples is likely due to matrix effects, in which coexisting ions and organic constituents compete with *o*-NP for active adsorption sites.

5.3. Comparison with other adsorbents

The adsorption performance of the newly developed $SrSnFe_2O_4$@δ-MnO_2/BC_{KOH} composite was benchmarked against other reported adsorbents (Table 5). $SrSnFe_2O_4$@δ-MnO_2/BC_{KOH} exhibited superior adsorption capacity compared to many conventional materials. These results highlight its potential as a highly effective and practical adsorbent for environmental remediation applications.

6. Conclusion

The $SrSnFe_2O_4$@δ-MnO_2/BC_{KOH} composite derived from cotton stalk biochar shows strong potential as a sustainable, multifunctional adsorbent for removing *o*-nitrophenol (*o*-NP) from aqueous media. Incorporation of MnO_2 and $SrSnFe_2O_4$ improved the textural properties of biochar by increasing surface area and porosity and introduced magnetic functionality that facilitates separation and recovery. The composite exhibited high adsorption efficiency, rapid kinetics, and favourable isotherm behaviour, indicating strong affinity for *o*-NP. Although the saturation magnetisation decreased after composite formation, it remained adequate for magnetic separation. The material also maintained good performance in real wastewater, supporting its applicability under practical conditions, and demonstrated regeneration and reusability over multiple cycles. Overall, this work demonstrates the upcycling of agricultural residues into value-added magnetic biochar-based composites for the remediation of phenolic wastewater. Future studies should address scale-up, continuous-flow evaluation, and assessment against broader classes of contaminants.

Author contributions

Ahmed M. Abdelfatah was responsible for conducting the laboratory experiments, investigation, formal analysis, methodology, data curation, visualization, validation, resources, and writing the original draft. Manal Fawzy: suggested the idea of this article, conceptualization, funding acquisition, project administration, supervision, and reviewed the final manuscript. Mohamed E. El-Khouly: conceptualization, writing, review, editing, and supervision. Abdelazeem S. Eltaweil:

conceptualization, resources, writing, review, editing, formal analysis, visualization, and supervision.

Conflicts of interest

The authors declare that they have no competing interests.

Data availability

Data will be available on request.

Supplementary information (SI): detailed information on the chemicals used in the experimental work, materials characterization data, kinetic models, thermodynamic analysis (including the van't Hoff plot), XPS peak-fitting parameters, and the equations applied for adsorption kinetic and isotherm models. See DOI: https://doi.org/10.1039/d6ra00303f.

Acknowledgements

Open access funding provided by The Science, Technology & Innovation Funding Authority (STDF) in cooperation with The Egyptian Knowledge Bank (EKB). This research was supported by the Egyptian Science, Technology, & Innovation Funding Authority (STDF), grant number 45888 under the umbrella of the USAID/STDF collaborative project.

References

1 X. Liu, S. Shi, S. Wang, Z. Ren, Y. Wang, Q. Guo, S. Feng, Y. Li, J. Qu and Y. Zhang, *Environ. Res.*, 2025, **286**, 122761.
2 R. Liu, W. Ji, W. Wang, Y. Li, L. Yin, Y. Song and G. He, *Sep. Purif. Technol.*, 2025, **361**, 131349.
3 N. Ghafourian, S. N. Hosseini, Z. Mahmoodi, N. Masnabadi, M. R. Thalji, A. R. Abhari, W. Al Zoubi, K. F. Chong, G. A. M. Ali and Z. H. Bakr, *Emergent Mater.*, 2023, **6**, 1527–1536.
4 J. Y. Lu, Z. Q. Bu, Y. Q. Lei, D. Wang, B. He, J. Wang and W. T. Huang, *J. Mol. Liq.*, 2024, **409**, 125503.
5 A. S. Eltaweil, E. Talaat, E. M. Abd El-Monaem and G. M. El-Subruiti, *J. Solid State Chem.*, 2025, **343**, 125159.
6 A. S. Eltaweil, K. Samir, E. M. Abd El-Monaem and G. M. El-Subruiti, *RSC Adv.*, 2025, **15**, 33549–33560.
7 A. S. Eltaweil, N. Al Harby, M. El Batouti and E. M. Abd El-Monaem, *RSC Adv.*, 2026, **16**, 1697–1713.
8 F. Jiang, Y. Zhang, X. Xu, Y. Mao, M. Wang, B. Yang, C. Zhang, X. Feng, H. Meng, F. Guo, Q. Han and S. Zhang, *J. Environ. Chem. Eng.*, 2025, **13**, 117556.
9 J. Qu, Y. Wang, X. Tian, Z. Jiang, F. Deng, Y. Tao, Q. Jiang, L. Wang and Y. Zhang, *J. Hazard. Mater.*, 2021, **401**, 123292.
10 D. C. C. da Silva Medeiros, M. Usman, P. Chelme-Ayala and M. Gamal El-Din, *Energy Environ. Sustainability*, 2025, **1**, 100028.
11 P. Choudhury, M. S. Manna and S. Nag, *Biomass Bioenergy*, 2025, **198**, 107859.
12 Ö. Arar, *Curr. Nanomater.*, 2025, **10**, 156–166.
13 Y. Ding, W. Xue, K. Chen, C. Yang, Q. Feng, D. Zheng, W. Xu, F. Wang and X. Lu, *Nanomaterials*, 2023, **13**, 1075.
14 A. Li, S. Lei, S. Chen, X. Zhou, Z. Wu, F. Jiang, P. Zheng, L. Hu and H. Deng, *Iscience*, 2025, **28**, 113991.
15 P. Prasad, C. R. Gordijo, A. Z. Abbasi, A. Maeda, A. Ip, A. M. Rauth, R. S. DaCosta and X. Y. Wu, *ACS Nano*, 2014, **8**, 3202–3212.
16 K.-W. Jung, S. Y. Lee and Y. J. Lee, *Bioresour. Technol.*, 2018, **261**, 1–9.
17 Y. Yao, L. Zhang, Y. Qiu, Z. Li, Z. Ma and S. Wang, *Water Res.*, 2024, **264**, 122224.
18 K. Liu, Q. Wang, Q. Wu, F. Zhang, L. Li and H. Zheng, *Ceram. Int.*, 2025, **51**, 28726–28735.
19 M. I. Din, S. Rehman, Z. Hussain and R. Khalid, *Rev. Inorg. Chem.*, 2024, **44**, 91–116.
20 K. M. Shakhidoyatov, A. Rashkes and N. Khidyrova, *Chem. Nat. Compd.*, 1997, **33**, 605–616.
21 A. A. Bell, *Cotton Physiology*, The Cotton Foundation, Memphis, TN, 1986, pp. 597–621.
22 N. Haleem, M. Arshad, M. Shahid and M. A. Tahir, *Carbohydr. Polym.*, 2014, **113**, 249–255.
23 A. M. Abdelfatah, M. Fawzy, M. E. El-Khouly and A. S. Eltaweil, *Biomass Convers. Biorefin.*, 2025, **15**(17), 24195–24213.
24 L. P. Lingamdinne, G. K. R. Angaru, C. A. Pal, J. R. Koduru, R. R. Karri, N. M. Mubarak and Y.-Y. Chang, *Sci. Rep.*, 2024, **14**, 4267.
25 J.-W. Wang, Y. Chen and B.-Z. Chen, *J. Electrochem. Soc.*, 2015, **162**, A1654.
26 N. O. M. Dewi and Y. Yulizar, *Mater. Today: Proc.*, 2020, **22**, 199–204.
27 I. K. Durukan, I. Ulu and Ö. Dag, *J. Mater. Chem. A*, 2024, **12**, 6359–6375.
28 A. M. Omer, M. El-Sayed, E. M. Abd El-Monaem, G. M. El-Subruiti and A. S. Eltaweil, *Int. J. Biol. Macromol.*, 2023, **253**, 127437.
29 P. Dubey, P. Sharma and V. Kumar, *Data Brief*, 2017, **15**, 615–622.
30 N. Atykyan, V. Revin and V. Shutova, *AMB Express*, 2020, **10**, 84.
31 K. Břendová, J. Száková, M. Lhotka, T. Krulikovská, M. Punčochář and P. Tlustoš, *Environ. Geochem. Health*, 2017, **39**, 1381–1395.
32 K. Břendová, J. Száková, M. Lhotka, T. Krulikovská, M. Punčochář and P. Tlustoš, *Environ. Geochem. Health*, 2017, **39**, 1381–1395.
33 K. Jedynak and B. Charmas, *Adsorption*, 2024, **30**, 167–183.
34 P. Ajithkumar, S. Mohana and S. Sumathi, *J. Mater. Sci.: Mater. Electron.*, 2020, **31**, 1168–1182.
35 I. Mansuri, R. Farzana, R. Rajarao and V. Sahajwalla, *Metals*, 2018, **8**, 290.
36 A. M. Dehkhoda, E. Gyenge and N. Ellis, *Biomass Bioenergy*, 2016, **87**, 107–121.
37 M. Zahan and J. Podder, *SN Appl. Sci.*, 2020, **2**, 385.
38 P. Ajithkumar, S. Mohana and S. Sumathi, *J. Mater. Sci.: Mater. Electron.*, 2020, **31**, 1168–1182.
39 F. A. Alharthi and I. Hasan, *J. Mater. Sci.: Mater. Electron.*, 2023, **34**, 2281.

40 J. Yang, S. Ren, B. Su, Y. zhou, G. Hu, L. Jiang, J. Cao, W. Liu, L. Yao, M. Kong, J. Yang and Q. Liu, *Catal. Lett.*, 2021, **151**, 2964–2971.
41 X. Huang, W. Cui, J. Yu, S. Lu and X. Liao, *Catal. Lett.*, 2022, **152**, 1441–1450.
42 X. Chen, S. Yan, N. Wang, S. Peng, C. Wang, Q. Hong, X. Zhang and S. Dai, *RSC Adv.*, 2017, **7**, 55734–55740.
43 F. Zheng, Z. Fang, M. A. Gaikwad, S. Jang and J. H. Kim, *J. Mater. Sci.: Mater. Electron.*, 2025, **36**, 960.
44 C. Julien, M. Massot, R. Baddour-Hadjean, S. Franger, S. Bach and J. Pereira-Ramos, *Solid State Ionics*, 2003, **159**, 345–356.
45 H. Xu, M. Liu, J. Hu and Y. Wang, *Ceram. Int.*, 2026, DOI: 10.1016/j.ceramint.2026.01.053.
46 Q. Li, C. W. Kartikowati, S. Horie, T. Ogi, T. Iwaki and K. Okuyama, *Sci. Rep.*, 2017, **7**, 9894.
47 W. Barthlott, M. Mail, B. Bhushan and K. Koch, *Nano-Micro Lett.*, 2017, **9**, 23.
48 D. Angın, E. Altintig and T. E. Köse, *Bioresour. Technol.*, 2013, **148**, 542–549.
49 T. C. Chandra, M. M. Mirna, J. Sunarso, Y. Sudaryanto and S. Ismadji, *J. Taiwan Inst. Chem. Eng.*, 2009, **40**, 457–462.
50 F. Yang, L. Zhao, B. Gao, X. Xu and X. Cao, *Environ. Sci. Technol.*, 2016, **50**, 2264–2271.
51 S. O. Amusat, T. G. Kebede, E. N. Nxumalo, S. Dube and M. M. Nindi, *Bioresour. Technol. Rep.*, 2022, **19**, 101160.
52 D. Fang, F. He, J. Xie and L. Xue, *J. Wuhan Univ. Technol., Mater. Sci. Ed.*, 2020, **35**, 711–718.
53 H. Idriss, *Surf. Sci.*, 2021, **712**, 121894.
54 P. S. Bagus, C. J. Nelin, C. Brundle, B. V. Crist, N. Lahiri and K. M. Rosso, *Phys. Chem. Chem. Phys.*, 2022, **24**, 4562–4575.
55 E. S. Ilton, J. E. Post, P. J. Heaney, F. T. Ling and S. N. Kerisit, *Appl. Surf. Sci.*, 2016, **366**, 475–485.
56 A. Wieczorek, H. Lai, J. Pious, F. Fu and S. Siol, *Adv. Mater. Interfaces*, 2023, **10**, 2201828.
57 S. Komai, M. Hirano and N. Ohtsu, *Surf. Interface Anal.*, 2020, **52**, 823–828.
58 R. Sawyer, H. Nesbitt and R. Secco, *J. Non-Cryst. Solids*, 2012, **358**, 290–302.
59 S. U. Din, P. T. Ngueagn, K. M. Al-Ahmary, H. AlMohamadi, S. R. Al-Mhyawi, N. Y. Elamin, I. F. Alshdoukhi, J. S. Alrashood and E. A. Ofudje, *Sci. Rep.*, 2025, **15**, 31659.
60 A. H. Jawad, A. S. Abdulhameed, S. Surip and Z. A. Alothman, *J. Cleaner Prod.*, 2023, **393**, 136334.
61 M. Li, J. Mu, Y. Liu, H. Wang, Y. Wang and H. Song, *Res. Chem. Intermed.*, 2023, **49**, 2209–2232.
62 M. Shahabi Nejad, H. Soltani Nejad, S. Arabnejad and H. Sheibani, *J. Appl. Polym. Sci.*, 2021, **138**, 50962.
63 N. M. Gaber, G. M. El-Subruiti, A. M. Omer and A. S. Eltaweil, *Surf. Interfaces*, 2024, **51**, 104528.
64 X. Li, J. Shen, Z. Sun, Y. Liu, W. Zhang, B. Wu, F. Ma and Q. Gu, *J. Environ. Chem. Eng.*, 2021, **9**, 106048.
65 M. Yang and M. Wang, *Prog. React. Kinet. Mech.*, 2018, **43**, 189–200.
66 A. Ahmadi, M. Hajilou, S. Zavari and S. Yaghmaei, *J. Cleaner Prod.*, 2023, **382**, 134967.
67 P. Kumari, K. M. Tripathi, K. Awasthi and R. Gupta, *Ind. Eng. Chem. Res.*, 2023, **62**, 19801–19812.
68 G.-W. Xu, Y.-H. Shen, Y.-L. Shan, J.-W. Ding, J.-K. Zhang and W.-L. Yu, *Sep. Purif. Technol.*, 2025, **354**, 128901.
69 L. Liu, G. Deng and X. Shi, *Sci. Rep.*, 2020, **10**, 5149.
70 X. Liu, S. Shi, S. Wang, Z. Ren, Y. Wang, Q. Guo, S. Feng, Y. Li, J. Qu and Y. Zhang, *Environ. Res.*, 2025, 122761, DOI: 10.1016/j.envres.2025.122761.
71 M. Akomolede, O. Omuvwie, A. Adeyi, I. Olateju, M. Omofoyewa, J. Ajayi and A. Giwa, 2025.
72 A. H. Mansee, D. M. Abdelgawad, E. H. El-Gamal, A. M. Ebrahim and M. E. Saleh, *Sci. Rep.*, 2023, **13**, 19153.
73 P. Alimohammadi, M. S. Nejad, M. R. Miroliaei and H. Sheibani, *Chem. Eng. Process.*, 2022, **176**, 108971.
74 F. Li, P. Fei, B. Cheng, J. Meng and L. Liao, *Carbohydr. Polym.*, 2019, **216**, 312–321.
75 Y. Chen, D. Wang, X. Wang, J. Wu and S. Song, *Sustainable Environ. Res.*, 2025, **35**, 4.